



Attachment of solid elongated particles on the surface of a stationary gas bubble



Gregory Lecrivain^{a,b,*}, Giacomo Petrucci^{b,c}, Martin Rudolph^d, Uwe Hampel^{b,e}, Ryoichi Yamamoto^a

^a Kyoto University, Department of Chemical Engineering, Kyoto 615-8510, Japan

^b Helmholtz-Zentrum Dresden-Rossendorf, Institute of Fluid Dynamics, Bautzner Landstraße 400, 01328 Dresden, Germany

^c Università di Modena e Reggio Emilia, Dipartimento di Ingegneria "Enzo Ferrari", Via Vignolese, 905/B, 41125 Modena, Italy

^d Helmholtz-Zentrum Dresden-Rossendorf, Helmholtz-Institute Freiberg for Resource Technology, Halsbrücker Str. 34, 09599 Freiberg, Germany

^e Technische Universität Dresden, Institut für Energietechnik, AREVA-Stiftungsprofessur für Bildgebende Messverfahren für die Energie- und Verfahrenstechnik, 01062 Dresden, Germany

ARTICLE INFO

Article history:

Received 30 September 2014

Received in revised form 27 December 2014

Accepted 9 January 2015

Available online 22 January 2015

Keywords:

Froth flotation

Three-phase system

Solid elongated particles

Particle attachment

Gas–liquid interface

ABSTRACT

Froth flotation is a separation process which plays a major role in the mining industry. It is essentially employed to recover a vast array of different valuable commodities such as rare earth minerals essential to the manufacture of high-tech products. Owing to its simplicity, the process is also widely used for the de-inking of recycled paper fibres and for the removal of pollutants from waste water. The flotation process essentially relies on the attachment of solid particles on the surface of gas bubbles immersed in water. The present study seeks to investigate the effect of the particle shape on the attachment mechanism. Using an in-house optical micro-bubble sensor the approach, the sliding and the adhesion of micron milled glass fibres on the surface of a stationary air bubble immersed in stagnant water is thoroughly investigated. The translational and rotational velocities were measured for fibres of various aspect ratios. The results are compared with a theoretical model and with experimental data obtained with spherical glass beads. It is found that the fibre orientation during the sliding motion largely depends on the collision area. Upon collision near the upstream pole of the gas bubble the major axis of the fibre aligns with the local bubble surface (tangential fibre alignment). If collision occurs at least 30° further downstream only head of the fibre is in contact with the gas–liquid interface (radial fibre alignment).

© 2015 Elsevier Ltd. All rights reserved.

Introduction

Motivation

Froth flotation is a versatile separation process which plays a major role in the mining industry. It is essentially employed to recover a vast array of different valuable commodities such as copper, zinc, nickel, phosphate and rare earth minerals essential to the manufacture of high-tech products (Fuerstenau et al., 2007). Owing to its simplicity, the process has more recently seen widespread applications in the non-mining field. Flotation is for instance used for the de-inking of recycled paper fibres (Kemper, 1999) and for the removal of pollutants from waste water (Rubio et al., 2002). In mineral froth flotation the separation can be accomplished in a flotation cell, which is essentially a tank fitted with an impeller

(Ahmed and Jameson, 1985). The impeller disperses air into fine gas bubbles and agitates the slurry. It provides a favourable environment in the cell for the promotion of bubble collision with the finely ground ore (Fuerstenau et al., 2007). Typical values of particle diameters, for which the recovery rate is high, vary from approximately $d_p = 10 \mu\text{m}$ to $d_p = 150 \mu\text{m}$. (Tao, 2005; Jameson, 2010). Many ore minerals are naturally hydrophilic. The addition of so-called “collectors” to the slurry, which are absorbed by the mineral surface, renders the precious mineral particles hydrophobic (Rosenqvist, 2004). The hydrophobised particles then attach to the surface of the rising bubbles, whose size generally ranges from $d_b = 0.6$ to 2 mm in diameter (Rubio et al., 2002). The particle-bubble aggregates are conveyed to the top of the flotation cell to form a rich mineral-laden froth layer, which eventually overflows into a launder as a separate product. Since pure liquids generally do not foam, “frothers” are utilised to control the bubble size and to stabilise the froth (Cho and Laskowski, 2002). The gangue, i.e. the commercially valueless hydrophilic material, eventually exits the flotation cell as slurry.

* Corresponding author at: Kyoto University, Department of Chemical Engineering, Kyoto 615-8510, Japan. Tel./fax: +81 (0)75 383 2651.

E-mail address: g.lecrivain@hzdr.de (G. Lecrivain).

Particle shape

Ore grinding in froth flotation is an important step to liberate the valuable mineral particles from the gangue (Forssberg et al., 1993). Kursun and Ulusoy (2006) showed for instance that the shape of talc mineral particles produced by milling considerably deviated from an ideal sphere. Talc minerals ground by rod milling showed higher elongation and flatness than those ground by ball milling. The study of Rahimi et al. (2012) also suggested that rod milling caused an elongation of the particles and that ball milling caused a greater particle roundness. Various studies have shown that the particle elongation increases the recovery rate. Koh et al. (2009) found that ground ballotini particles had a higher recovery rate than spherical ballotini particles. The work of Yekeler et al. (2004) also corroborated this finding. The team experimentally observed that particle elongation increased the ease, with which a particle attaches to a bubbles surface. Particle roundness tended to have an adverse effect on the recovery rate. Note, that the recovery rate k is the rate at which the desired particles are recovered from the suspension. In a flotation tank, the number concentration $c(t)$ of the desired particles will decay exponentially with time. Ahmed and Jameson (1985) suggested the following formula $c(t) = c_0 \exp(-kt)$, where c_0 was the initial concentration in the tank.

Particle attachment on bubble surface

The attachment of a solid particle on the surface of a gas bubble can be divided into three successive stages: the particle approach, the collision with the bubble and the sliding down the gas–bubble interface (Schulze, 1989; Albijanic et al., 2010). The downward sliding motion of the particle is caused by the gravity and also by the hydrodynamic forces arising from the local water flow around the rising bubble. Should the particle approach the bubble surface within the range of attractive surface forces, a thin intervening liquid film between the gas–liquid interface and the solid–liquid interface forms. The liquid film eventually drains, leading to a critical thickness at which rupture occurs (Ralston et al., 1999). The rupture of the liquid film results in the formation of a stable three-phase contact (Schulze, 1992). The deployment of high speed camera systems has been favoured in recent years to observe the particle attachment in great detail. Wang et al. (2003a) photographically recorded the attachment of free falling spherical glass beads on a stationary air bubble, which had undergone various surface treatments. Gu et al. (2004) investigated the attachment of rising spherical hydrogen bubbles on a larger fixed bitumen particle. Hubička et al. (2013) measured the trajectories of an approaching large solid spherical particle on a stationary gas bubble. The sliding was however left out by the authors. Verrelli et al. (2014) were the first to look at the attachment of non-spherical particles. They measured the induction time, i.e. the time required for the liquid film to thin to its critical film thickness (Ye et al., 1989), of ‘angular frit’ particles falling on a gas bubble. The above state of the art clearly shows that the attachment process has largely been limited to the attachment of perfectly spherical particles. The effect of shape irregularity on the attachment process has received scarce attention. To date only one attempt can be found in the literature. The present piece of work aims to alleviate this shortcoming by experimentally investigating the attachment of elongated particles with an aspect ratio of up to 7.

Methods

Experimental facility

The experimental procedure employed to visualise attachment of solid particles was inspired by the work of Verrelli et al.

(2014). As illustrated in Fig. 1 the experimental set-up essentially consisted of water tank in which a needle was placed in a horizontal position. The 25 gauge ultra-smooth hydrophobic needle with a ta-C diamond-like carbon coating (SGE Analytical Science, Diamond MS Syringe 0355321) was attached to a 50 μ l precision syringe (Hamilton, 1805RNSYR). It allowed blowing a stable and stationary air bubble, whose diameter could be varied from $d_b = 1.3$ mm to $d_b = 1.7$ mm. A larger bubble diameter resulted in a detachment of the gas bubble from the needle. The adhesion force holding the bubble on the needle tip could no longer overcome the buoyancy force. The present bubble size range matched the typical size range frequently found in the literature (Huang et al., 2011). The water was kept at a constant room temperature of 20 °C and had a pH value of 7.8. The opened-water tank was made of transparent Plexiglas walls. A tube fastened in a vertical position had its immersed extremity placed 15 mm away from the bubble upper pole (henceforth referred to as the upstream pole), which corresponded to a distance of about 10 bubble diameters. The reason behind the use of the fastened vertical tube was threefold: 1. to guide the particles all the way down to the gas bubble, 2. to avoid an interference of the falling particle with the surrounding liquid and 3. to hold the Pasteur pipette in a stable vertical position. The Pasteur pipette, containing the particles heavily diluted in water, could then be placed in the tube in question. The bulb of the pipette in contact with ambient air was pierced to avoid a squeezing that would potentially give the particles an undesired acceleration. By releasing the finger from the bulb the solid particles could start their decent with an initial velocity close to zero. The present facility unfortunately did not exactly reproduce all mechanisms observed in an industrial flotation cell. The motion of the liquid and of the gas phases were here left out, and so were the effect of frother and collector addition. To the best of the authors’ knowledge the present study, even though it is a fairly simple system, is the first of its kind that seeks to investigate the effect of particle elongation on the overall attachment mechanism, which is of chief importance in the flotation process. It is hoped that the present results will help build more complex models in the future.

Solid particles

Experimental tests were performed with spherical particles for comparison purposes and fibre-like elongated particles. The glass spherical particles (Wiwox, STGP002) had a particle-to-liquid density ratio of $S = \rho_s/\rho_l = 2.45$ and a diameter ranging from $d_p = 50$ μ m to $d_p = 100$ μ m. The milled glass fibres (3B-Fibreglass, MF01ER) had a particle-to-liquid density ratio of $S = 2.5$ and a length ranging from 100 μ m to 200 μ m in the long-axis direction (major axis). Detailed images of the elongated particles obtained

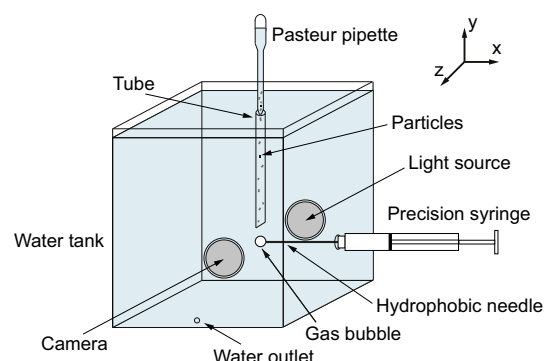


Fig. 1. Schematic of the test facility.

from the on-site Scanning Electron Microscope which operates under high vacuum conditions (Zeiss EVO 50) revealed an aspect ratio, defined as the ratio of fibre length to diameter, ranging from $e = 1$ to $e = 7$. Fig. 2a illustrates high-resolution images of spherical particles. The small structures on the surface of the elongated particles (Fig. 2b) are probably smaller glass particles. This highly polydispersity in the particle size distribution can be seen in Fig. 2c.

A spherical particle falling in stagnant water eventually reaches its terminal velocity

$$u_{\infty} = g \left(\frac{Sd_p^2}{18\nu} \right) \left(1 - \frac{1}{S} \right) = g\tau \left(1 - \frac{1}{S} \right), \quad (1)$$

where g is the gravity and $\nu = \mu/\rho_L$ is the liquid kinematic viscosity, i.e. the ratio of the liquid dynamic viscosity to the liquid density. The terminal velocity of a spherical particle can be conveniently expressed using the particle response time τ . This time corresponds to the time required by a particle to respond to a change in the liquid velocity (Crowe et al., 2011). The response time τ is defined as

$$\tau = \frac{Sd_p^2}{18\nu}. \quad (2)$$

For an elongated particle the terminal velocity will be affected by the orientation of the major axis relative to direction of motion. In the present work the direction of motion simply coincides with the direction of the gravity g since the liquid is at rest. The terminal velocity of an elongated particle with an aspect ratio of $e = 6$ will differ by up to 60% to that of a spherical particle with equivalent volume (Kasper et al., 1985). Further analysis on the terminal velocity of an elongated particle is dealt with in greater detail in the discussion section.

Particle hydrophobicity

The determination of the particle hydrophobicity is not straightforward and often requires special instrumentation. The sessile method, one of the simplest available methods, which involves the optical measurement of the contact angle of a droplet at rest on a substrate, will often fail for powder (Susana et al., 2012). In addition the sole determination of the contact angle between a solid surface and a gas–liquid interface does not allow for the exact description of the surface hydrophobicity since specific and aspecific interactions need to be considered. Consequently, two surfaces with the same contact angle with water can actually have a different hydrophobicity (van Oss, 2003). To overcome this, inverse gas chromatography (Mohammadi-Jam and Waters, 2014) was presently used to measure the specific surface free energies of the two sets of powder previously described in

Section “Solid particles”. The inverse gas chromatography measurement device (Surface Energy Analyser, Surface Measurement Systems) was here used for determination of the disperse component γ^d , the Lewis acid component γ^+ and the Lewis base component γ^- of the specific surface free energy at surface coverages of 1%, of 20% and of an extrapolation to 100% (Das et al., 2011; Gamble et al., 2012). The variation in the percentage of the surface coverage allowed an assessment of the heterogeneity in the surface energy. The total surface free energy was then calculated as follows

$$\gamma^t = \gamma^d + 2\sqrt{\gamma^+\gamma^-}. \quad (3)$$

Prior to the determination of the surface free energy at different surface coverages, the specific surface area of the two sets of particles per unit mass S_m^{BET} were determined with the N₂-BET method (Brunauer et al., 1938) using special instrumentation (FlowSorb II 2300, Micromeritics). The specific surface area per unit mass helped determine the amount of probe gases needed for a given surface coverage. For the determination of the disperse component heptane, octane, nonane and decane probe gas molecules were carried by a helium gas flowing at a rate of 10 cm³/min. Monopolar ethyl acetate was used for the determination of the Lewis acid component and dichloromethane for the Lewis base, respectively. The column was operated at 0% humidity and at a 90 °C temperature to ensure a clean surface, which in-turn guaranteed a desorption throughout the entire measurement procedure. A mass sample was chosen so that the surface area equalled 0.5 m². The samples were tapped vertically for ten minutes in a 3-mm inner diameter and 30-cm length column, which was sealed with inert silanized glass wool. Prior to the measurement the samples were conditioned at a 100 °C temperature for a period of 5 h in a helium gas also flowing at 10 cm³/min. The specific surface free energy components were calculated using the peak maximum of the probe molecule retention. The Schultz approach was employed for the disperse component γ^d , the van Oss-Chaudhury-Good/Della-Volpe approach for the Lewis acid/basic component (Das et al., 2011). To thermodynamically evaluate whether the particle attachment to a gas bubble is actually favourable in liquid water the specific free energy of interaction ΔG_{pwb} was calculated as follows (van Oss, 2003)

$$\begin{aligned} \Delta G_{pwb} = & \left(\sqrt{\gamma_S^d} - \sqrt{\gamma_G^d} \right)^2 - \left(\sqrt{\gamma_S^d} - \sqrt{\gamma_L^d} \right)^2 - \left(\sqrt{\gamma_G^d} - \sqrt{\gamma_L^d} \right)^2 \\ & + 2 \left(\sqrt{\gamma_L^+} [\sqrt{\gamma_S^+} + \sqrt{\gamma_G^+} - \sqrt{\gamma_L^+}] + \sqrt{\gamma_L^-} [\sqrt{\gamma_S^-} + \sqrt{\gamma_G^-} - \sqrt{\gamma_L^-}] \right. \\ & \left. - \sqrt{\gamma_S^+ \gamma_G^+} - \sqrt{\gamma_p^+ \gamma_G^+} \right). \end{aligned} \quad (4)$$

The subscript L , G and S respectively denote the specific free surface energies of the liquid water (L), of the gas bubble (G) and of the solid particles (S). Finally the contact angle θ between the particle surface

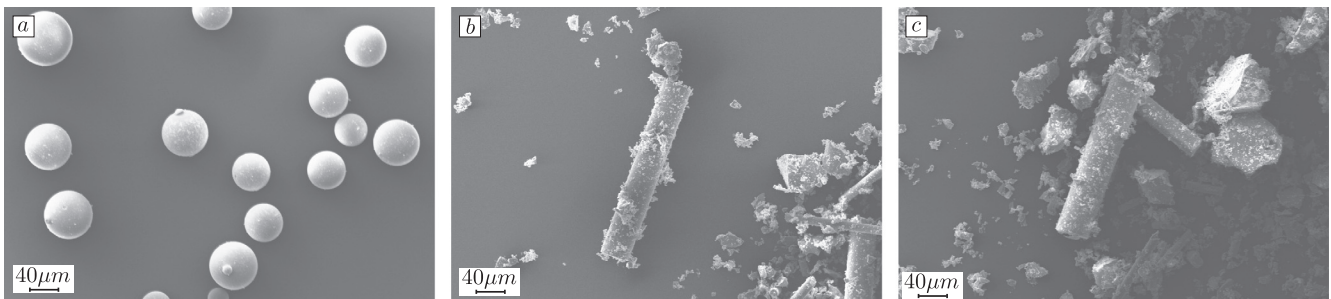


Fig. 2. Images of the spherical (a) and elongated particles (b and c) obtained with scanning electron microscope.

and the liquid water was determined using the surface free energy components as follows (van Oss, 2003)

$$\theta = \cos^{-1} \left(\frac{2}{\gamma_L^t} \cdot \left[\sqrt{\gamma_S^d \gamma_L^d} + \sqrt{\gamma_S^+ \gamma_L^-} + \sqrt{\gamma_S^- \gamma_L^+} \right] - 1 \right) \quad (5)$$

The results are summarised in Table 1. The three components of the total specific energy for the air bubble and for the liquid water were taken from the literature (van Oss et al., 2005; VDI-GVC, 2013). Findings from the present inverse gas chromatography measurements show that, for the two sets of particles and under all surface coverages, the specific free energy ΔG_{pwb} is always negative and thus attachment is favourable in all cases. Thermodynamically speaking, the particles are indeed hydrophobic. Irrespective of the surface coverage, the specific free energy ΔG_{pwb} shows little heterogeneity for the spherical particles and the values of the free specific interactions and of the contact angles are all similar. The same cannot be said for the elongated particles. At a surface coverage of 1% there is a higher polarity for the elongated particles, which resulted in smaller contact angles and a lower free energy of interactions with a bubble in water. Compared to the spherical particles the hydrophobicity at 10% and at 100% coverage is greater. It is expected from the present results that the elongated particles will attach to the gas bubble slightly differently. The study also revealed a contact angle lying in the range $60^\circ < \theta < 70^\circ$. Fuerstenau et al. (2007) showed that this contact angle is large enough to achieve a good floatability in the flotation process. The present contact angle slightly overestimates the values worked out by Tino et al. (1996) and by Nowak et al. (2013) who reported contact angles ranging from 50° to 60° . The calculation of their contact angles was performed using the sessile method, which involved a water droplet at rest on a glass substrate. Last but not least, even with a surface treatment involving for instance chlorotrimethylsilane, the contact angle of smooth spherical glass beads can only be increased to about 90° (Nowak et al., 2013), therefore it is very hard to render glass particles fully hydrophobic.

Measurement instrumentation

To observe the attachment of a solid particle on a gas bubble surface the in-house optical micro-bubble sensor (Ren et al., 2011) developed at the Helmholtz Zentrum Dresden-Rossendorf was put to use in the present study. The sensor consists of two tubular waterproof housings facing each other's extremities. The gas bubble was placed between the two tubular shafts partly immersed in water. A distance of about 40 mm, which corresponded to about 25 bubble diameters, separated the two shafts. The first housing enclosed the CCD camera and the second enclosed the LED illumination system. The light source flashed in synchronisation with the camera exposure. A focus length of 20 mm allowed for a field of view of about $3.5 \times 2.6 \text{ mm}^2$, which was large enough to hold the gas bubble and capture the entire

particle attachment. Each image had a resolution of 640×480 pixels. With a particle terminal velocity ranging from $u_\infty = 1.5 \text{ mm/s}$ to $u_\infty = 7 \text{ mm/s}$ (see Annex 1) and a frame rate of 120 images per second it resulted in a local particle displacement between two consecutive illumination pulses ranging from $10 \text{ }\mu\text{m}$ to $60 \text{ }\mu\text{m}$.

Experimental data processing

The footage of a particle attachment was a very tedious task. The particle had to evolve over the course of the entire attachment process in the focus plane of the micro-bubble sensor. The attachment of a fibre was an even unlikelier event since the major axis also had to remain in the plane of focus so that the particle orientation could be determined. The chance of capturing the attachment of a very single particle was actually low. The facility did not allow the release of one particle at a time. Therefore only the head of the falling cloud, which had a local dilution greater than that of the bulk of the cloud, was here of interest. The reason behind the footage of the cloud head was twofold: (1) the chance of capturing single attachment in the field of view was increased and (2) the particle-induced flow and the inter-particle collisions near the gas bubble, which were observed to affect the attachment, could be avoided. While it was difficult to accurately estimate the occurrence of an exploitable attachment, we found out that about 50 experimental test runs resulted in one exploitable attachment. A measurement campaign lasting several weeks was therefore necessary to capture the 30 attachments of elongated particles and the 4 attachments of spherical particles presented in the present work. Each successful capture of a particle attachment, in which the particle evolved in the focus plane, was exported in the form of an image sequence to the post-processing program Fiji. The image processing program is an open-source platform normally used for biological-image analysis (Schindelin et al., 2012). After the threshold of each image sequence, a circle was fit to the gas bubble and polar coordinate system was defined. The diameter of the needle, which was of course known beforehand, was used as the reference length. During the approach the orientation of the major particle axis and its velocity could be automatically detected by fitting a two-dimensional ellipsoid. However during the sliding the particle shape could no longer be automatically discriminated from the gas bubble shadow. For this reason the determination of the major axis and the velocities were done manually for various images. It resulted in a time-consuming image processing.

Spherical particle transport model

The present experimental investigation was carried with "clean" bubbles, i.e. the gas-liquid interface underwent no contamination by frothers, which were previously found to significantly influence the collision efficiency (Sarrot et al., 2005). Further information on the effect of partial and full interface

Table 1
Measured hydrophobicity of the spherical particles and of the elongated particles at surface coverages of 1%, 10% and 100%.

Material	γ_m^{RET} (m ² /g)	Surface coverage	γ^d (mJ/m ²)	γ^- (mJ/m ²)	γ^+ (mJ/m ²)	γ^* (mJ/m ²)	ΔG_{pwb} (mJ/m ²)	θ (°)
Liquid water	–	–	18.0	21.1	21.1	60.2	–	–
Gas bubble	–	–	0.0	0.0	0.0	0.0	–	–
Spherical particles	0.069	1%	47.6 ± 3.5	3.5 ± 1.2	1.6 ± 0.3	52.2 ± 4.8	–33.3 ± 9.0	63.5 ± 6.7
		10%	49.3 ± 3.3	3.8 ± 1.2	0.9 ± 0.2	53.1 ± 4.4	–34.0 ± 8.8	64.2 ± 6.3
		100%	49.3 ± 3.4	3.5 ± 1.0	0.5 ± 0.2	52.1 ± 4.2	–36.8 ± 8.7	67.2 ± 5.8
Elongated particles	0.470	1%	37.4 ± 0.3	4.6 ± 0.1	4.0 ± 0.0	46.0 ± 0.4	–30.3 ± 3.4	60.2 ± 0.6
		10%	40.8 ± 0.6	3.3 ± 0.2	1.0 ± 0.1	44.5 ± 0.8	–40.0 ± 4.0	70.4 ± 1.2
		100%	40.8 ± 0.9	3.0 ± 0.2	1.1 ± 0.1	44.4 ± 1.1	–40.7 ± 4.4	71.1 ± 1.4

contamination on the collision efficiency can be found in the study of Legendre et al. (2009). The physico-chemical interfacial forces normally prevail over the hydrodynamic forces only within a very short distance from the gas–liquid interface, typically for a gap value lower than $h < 0.1 \mu\text{m}$ (Huang et al., 2012): a distance by several order of magnitude smaller than the particle size. Since the physic-chemical interfacial forces have little effect on the collision they were here left out. The history force and the lift force are of second order and can also be neglected (Nguyen, 2003). The effect of the Basset force even though it was included in the Lagrangian particle model of Verrelli et al. (2011) is often left out in other numerical studies (Nguyen and Nguyen, 2009). Thus retaining only the hydrodynamic drag exerted by the liquid phase, the gravity and the buoyancy, the vectorial transport equation of a point-like solid spherical particle evolving in the liquid phase therefore reads

$$m \frac{d\vec{u}}{dt} = -3\pi\mu d_p \vec{u} + (m - m_f) \vec{g}. \quad (6)$$

In the above equation \vec{u} is the particle velocity vector. Since the stationary bubble is immersed in stagnant water the velocity of the liquid phase is set to zero throughout the simulation. The term m corresponds to the particle mass and m_f to the mass of liquid displaced by the particle. The term μ corresponds to the dynamic viscosity of the liquid phase. The transport equation can conveniently be expressed in terms of the two polar coordinates (r, ϕ) , in which r is the distance from the bubble centre to the particle centre and ϕ the angle measured from the vertical axis (see Fig. 3). The polar axis $\phi = 0$ coincides with the upstream pole of the gas bubble. Using the terminal velocity u_∞ defined in Eq. (1) the polar transformation of Eq. (6) leads to the following system of scalar equations

$$\frac{du_r}{dt} = -\left[\frac{(1+k_s)f_r}{\tau}\right] u_r + \left[\frac{u_\phi^2}{r} - \frac{u_\infty}{\tau} \cos(\phi)\right], \quad (7)$$

$$\frac{du_\phi}{dt} = -\left[\frac{f_\phi}{\tau} + \frac{u_r}{r}\right] u_\phi + \left[\frac{u_\infty}{\tau} \sin(\phi)\right]. \quad (8)$$

The radial and tangential velocities are given by

$$u_r = \frac{dr}{dt}, \quad u_\phi = r \frac{d\phi}{dt}. \quad (9)$$

The particle will deviate from its original trajectory as it approaches the bubble surface. To account for the change in the particle motion towards the bubble side the hydrodynamic force requires an artificial correction. Since the particle size is much smaller than the bubble size, it can be assumed that the particle encounters a fairly flat gas–liquid interface (Nguyen and Jameson, 2005). The radial and tangential drag components are therefore corrected using the following polynomial approximations (Huang et al., 2012)

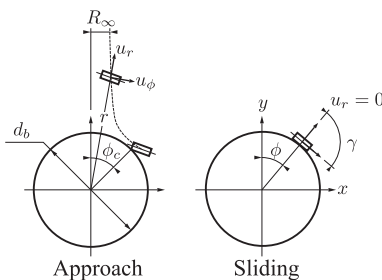


Fig. 3. Schematic representation of an elongated particle in its polar system during the approach and the sliding phase.

$$f_r = 1 + \frac{3}{2}\lambda + \frac{9}{4}\lambda^2 + \frac{19}{8}\lambda^3 + \frac{93}{16}\lambda^4 + \frac{387}{32}\lambda^5 + \frac{1197}{64}\lambda^6 + \frac{5331}{128}\lambda^7 + \frac{19821}{256}\lambda^8 + \frac{76115}{512}\lambda^9 + \frac{3}{10} \left[\frac{(2\lambda)^{10}}{1+2\lambda} \right], \quad (10)$$

$$f_\phi = 1 - \frac{3}{4}\lambda + \frac{9}{16}\lambda^2 - \frac{59}{64}\lambda^3 + \frac{465}{256}\lambda^4 - \frac{15813}{7168}\lambda^5 + 2 \left(\frac{\lambda^6}{1+\lambda} \right), \quad (11)$$

where the dimensionless variable λ equals $\lambda = 0.5d_p/(2h + d_p)$. The gap $h = r - 0.5(d_p + d_b)$ corresponds to smallest distance between the particle surface and the bubble surface. Close to the gas–bubble interface the particle typically experiences an increase in the hydrodynamic drag force and a decrease in the tangential force. Far from the bubble the two approximations f_r and f_ϕ are smoothly brought back to unity using a blending function to exactly achieve the correct terminal velocity u_∞ . The blending function is a smooth approximation of the Heaviside step function. It is here given by

$$H_V(h^*) = \frac{1}{2} \left(1 + \tanh \left[\frac{h^* - h_m^*}{\Delta h^*} \right] \right). \quad (12)$$

The upper script * indicates the normalisation of the gap with the reference scaling $(d_b/2)$ for a length variable, see Eq. (14). With the smoothing centre $h_m^* = 0.6$ and the smoothing radius of $\Delta h^* = 0.3$ the final correction then takes the form $f_{r,\phi} = H_V + (1 - H_V)f_{r,\phi}$. The effect of the blending function can be seen in Fig. 4. A cut off of the polynomial function to the 3rd order is also shown. The reduction of Eqs. (10) and (11) to a third-order polynomial will largely affect the radial drag correction close to the gas–bubble interface, i.e. within $h^* < 0.1$. As in the original model of Huang et al. (2012), the above 10th- and 6th-order polynomial approximations are here employed. Upon collision with the gas bubble the two drag correction factors no longer make sense and therefore they equal unity. The dimensionless friction factor k_s is introduced to correct the particle drag force during the sliding motion on the bubble surface. Wang et al. (2003a) suggested, as is the case here, $k_s = 0.03$ for untreated glass beads interacting with ‘clean’ bubbles. The value of k_s is however significantly affected by the use of collectors and frothers (Wang et al., 2003b). Methylated glass spheres showed an increase in the friction factor to $k_s = 0.1$. A gas bubble stabilised with sodium palmitic acid caused an increase in the friction factor to $k_s = 1$. The friction coefficient therefore needs particular attention since its value spans up to three orders of magnitude. During the approach the friction factor k_s is set to zero and the hydrodynamic drag force simply reduces to its well-known Stokes’ formulation in the far-bubble region. During the sliding, which begins when the gap h drops to zero, the particle is in equilibrium in the radial direction. It means that the capillary adhesion force, the centrifugal force and the radial component of the gravity cancel one another out and $u_r = 0$. An extensive analysis on the adhesion forces can be found in the discussion. An implicit Euler backward scheme is used for the numerical integration of the two transport equations (Eqs. (7) and (8)) and a standard second-order Adams–Bashforth scheme is applied to compute the particle displacement (Eq. (9)). These two integration schemes were previously found appropriate to accurately compute the transport and the deposition of micron-sized particles (Lecrivain and Hampel, 2012; Lecrivain et al., 2014).

Results and discussions

Model validation

The performance of the transport model for spherical particles is initially compared with four experimental reference runs, which all involved the glass beads of spherical shape. The four experimental tests were carefully selected so that the corresponding

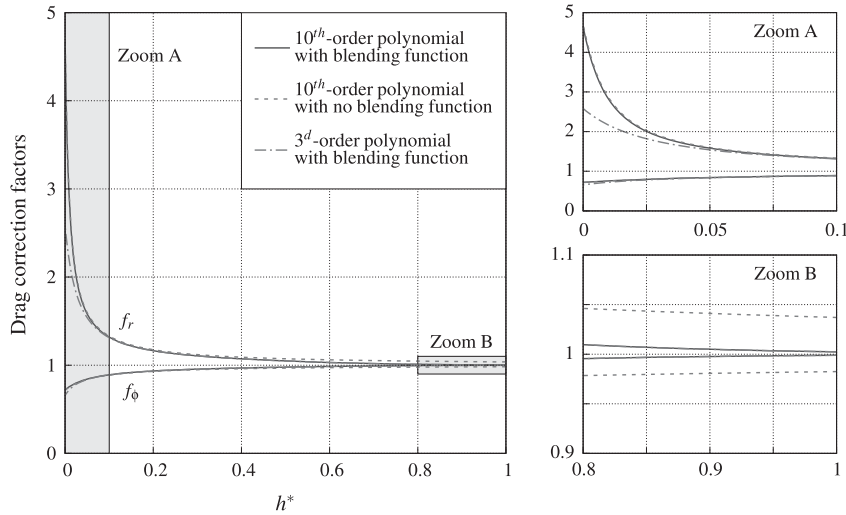


Fig. 4. Radial and tangential drag correction factors shown as a function of the gap.

collision angle ϕ_c of each run lied in one of the four collision intervals $I_{i=1...4}$.

$$\begin{aligned} I_1: & \phi_c < 10^\circ \\ I_2: & 10^\circ \leq \phi_c < 30^\circ \\ I_3: & 30^\circ \leq \phi_c < 50^\circ \\ I_4: & \phi_c \geq 50^\circ \end{aligned} \quad (13)$$

Fig. 5 presents the theoretical particle trajectories coloured by velocity magnitude with their experimental counterparts. At the initial simulation time $t = 0$ s, the particle velocity equals the terminal velocity calculated from Eq. (1) and the horizontal particle position $R(t = 0) = R_\infty$ equals that measured from the very first occurrence of the particle in the camera field of view. The distance R corresponds to the shortest distance from the particle centre to the vertical rotation axis of the bubble ($x = 0$). All lengths and velocity variables are henceforth made non-dimensional with the bubble radius and with the terminal velocity so that, irrespective of the changes in the bubble and particle sizes, all data can easily be compared with one another. The distance R , for instance, is normalised as follows

$$R^* = \frac{2R}{d_b}, \quad (14)$$

and the instantaneous particle velocity is normalised as follows

$$u^* = \frac{|\vec{u}|}{u_\infty}. \quad (15)$$

The terminal velocity is experimentally calculated from the two furthest upstream particle positions. It can be seen that the theoretical particle trajectories and the theoretical particle velocities agree qualitatively well with the experimental results. Because of the increase in the drag force and the decrease in the tangential force that the particle encounters during its approach near the gas–bubble interface the particle smoothly moves away from the vertical rotation axis of the bubble. The deviation of the particle trajectories can quantitatively be assessed with the collision angle ϕ_c . Using identical boundary conditions (d_p, d_b) and initial release conditions (u^*, R^*) it is found that the theoretical collision angles match remarkably well the experimental data in the three intervals $I_{i=1...3}$. The model however overestimates the deviation in the particle trajectory by about 15% for large collision angles. The reason behind the larger errors in the fourth interval I_4 is given in the next Section “Approach of the elongated particles”.

Approach of the elongated particles

The velocity magnitude of each falling elongated particle during the approach phase is compared with that obtained from the four experimental runs involving the spherical particles and that obtained from the theoretical model. Fig. 6 shows the velocity magnitude as a function of the polar coordinate r^* . Similarly to the model validation against the spherical glass bead data the results are sorted by collision angle and placed in one of the four collision intervals $I_{i=1...4}$ (Eq. (13)). In each of the four subdiagrams the abscissa r^* decreases to unity. This lower bound indicates a collision with the gas bubble surface. The results show that the velocity magnitude of the approaching particles is not significantly affected by the particle aspect ratio. It is a major finding since even a model for spherical particles can be employed to predict the translational velocities and the trajectories of elongated particles. In the far-bubble region, found to be the region in which the normalised polar radius is greater than $r^* > 1.8$, the bubble has little effect on the particle motion: each particle descends with a constant velocity equalled to the terminal velocity u_∞ . In the bubble region ($r^* < 1.8$) and for a collision angle lower than $\phi_c < 50^\circ$ the velocity magnitude rapidly decreases. The closer the collision near the upstream pole the greater the deceleration. Upon collision with an angle lower than $\phi_c < 10^\circ$ the particle experiences a loss in velocity of about 80% (interval I_1). In the third interval I_3 the particle experiences a loss in velocity of about 40%. As previously observed in the validation of the particle trajectories (Fig. 5) the model exhibits an unrealistic behaviour for large collision angles (interval I_4). In the fourth interval I_4 the theoretically determined velocity magnitude increases as the particle approaches the bubble surface. Further analysis of the simulation data showed a strong decrease in the tangential drag force component, which in-turn caused this unnatural increase in the particle velocity magnitude. It seems that, for large collision angles, the two drag corrections (Eqs. (10) and (11)) lose validity when the particle comes very close to the gas–bubble interface, i.e. within $r^* < 1.1$.

Sliding of the elongated particles

The velocity magnitude was also measured during the sliding phase. As illustrated in Fig. 7, it can be seen that the particle elongation does not influence the velocity magnitude in each collision interval. The model also performs remarkably well. The velocity magnitude reaches its maximum when the polar angle reaches

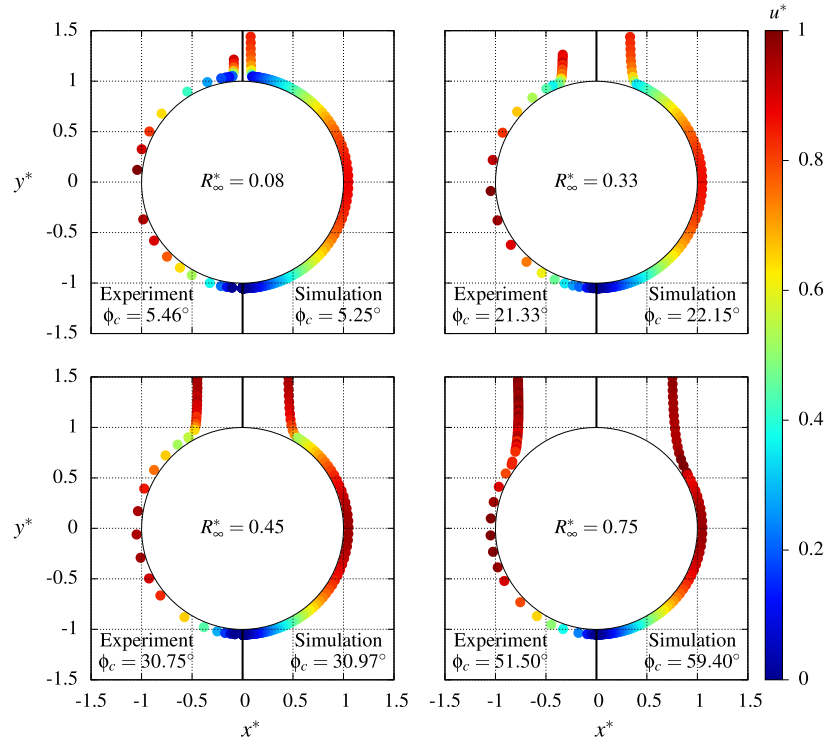


Fig. 5. Validation of simulated trajectories coloured by velocity magnitude. Simulations and experiments were performed with spherical particles.

100°. The orientation of the particle major axis with the radial direction is denoted by the angle γ (see Fig. 3 for an illustrative schematic). Fig. 8 illustrates the two types of ellipsoidal attachments: the “weak attachment” and the “strong attachment”. The weak attachment indicates a radial alignment of the fibre at the gas–liquid interface. Only one of the two fibre extremities eventually adheres to the gas–liquid interface ($\gamma = 0$ towards the end of the sliding). The strong attachment indicates a larger three-phase contact area. Throughout the sliding phase the particle major axis aligns with the gas–liquid interface ($\gamma = 90^\circ$) which results in a tangential alignment of the fibre at the gas liquid interface. The evolution of the major axis orientation as a function of the polar angle over the course of the sliding is shown in Fig. 9. The figure is divided into two subfigures. Fig. 9a on the left hand side encompasses the elongated particles for which a weak attachment was observed. Fig. 9b on the right hand side encompasses the elongated particles for which a strong attachment was observed. As expected the strong attachment involves a particle orientation which equals 90° throughout the entire attachment. During a weak attachment the elongated particle initially aligns with the bubble surface (tangential contact, $\gamma = 90^\circ$) and when the polar angle reaches the surface bubble region $90^\circ < \phi < 120^\circ$ the particle orientation suddenly changes: the alignment becomes radial ($\gamma = 0^\circ$). Last but not least, about 90% of experimental runs, in which the collision angle exceeded the threshold $\phi_c > 30^\circ$, resulted in a weak attachment (left Fig. 9a). Should the collision angle be lower than this threshold collision angle (grey area in the right Fig. 9b), the attachment was found take a strong form. The effect of the collision angle has a major effect on the fibre orientation during the sliding motion.

Discussions

Sliding time

The weak attachment is very likely due to the shorter time of “induction” (Yoon and Luttrell, 1989) which does not allow for the formation of a stronger tangential three-phase contact.

Verrelli et al. (2012) experimentally measured the induction time of methylated borosilicate glass spheres. The team showed that the induction time increased with the collision angle, i.e. a larger collision angle resulted in a longer time required for the film rupture to occur. For collision angles greater than $\phi_c > 30^\circ$ the team estimated an induction time ranging from 0.1 to 0.2 s. A collision near the upstream pole resulted in a lower induction time of about 0.02 s. During a weak attachment and irrespective of its shape, it was here found that a particle colliding with the bubble at a polar angle greater than $\phi_c > 30^\circ$ required on average 0.15–0.2 s to reach the bubble equator, after which the particle changed its orientation γ . The present sliding time needed to reach the bubble equator is of course determined for glass beads with a contact angle of $\theta = 60 - 70^\circ$ and can therefore not be directly compared with the induction time of glass particles with a surface treatment. Yet it seems that the sliding time needed to reach the bubble equator should be large enough for a strong attachment to occur.

Forces at the gas–liquid interface

Findings from this work along with the experimental observations of Wang et al. (2003b) have shown that the maximum value, for which the rotational velocity reaches its maxima, is not exactly found at 90° , but at a polar angle located between 90° and 110° . Surprisingly it fairly corresponds to the range, in which the particle suddenly changes its orientation γ over the course of a weak attachment (Fig. 9). Could it be that the change in the particle orientation during a weak attachment is triggered by the centrifugal force? It is therefore of interest to work out which forces prevail during the sliding process. The magnitude of the various forces are here derived from the theoretical work of Nguyen (2003). He developed a force balance model, in which a spherical particle is at rest at the downstream pole of a bubble, i.e. at $\phi = 180^\circ$. Four major static forces were identified: the capillary force F_{cap} , the buoyancy F_b , the pressure force F_p and the particle weight F_g . In the following each force is normalised with the surface tension σ and the capillary length $L = \sqrt{\sigma/(\rho_l g)}$. The mathematical

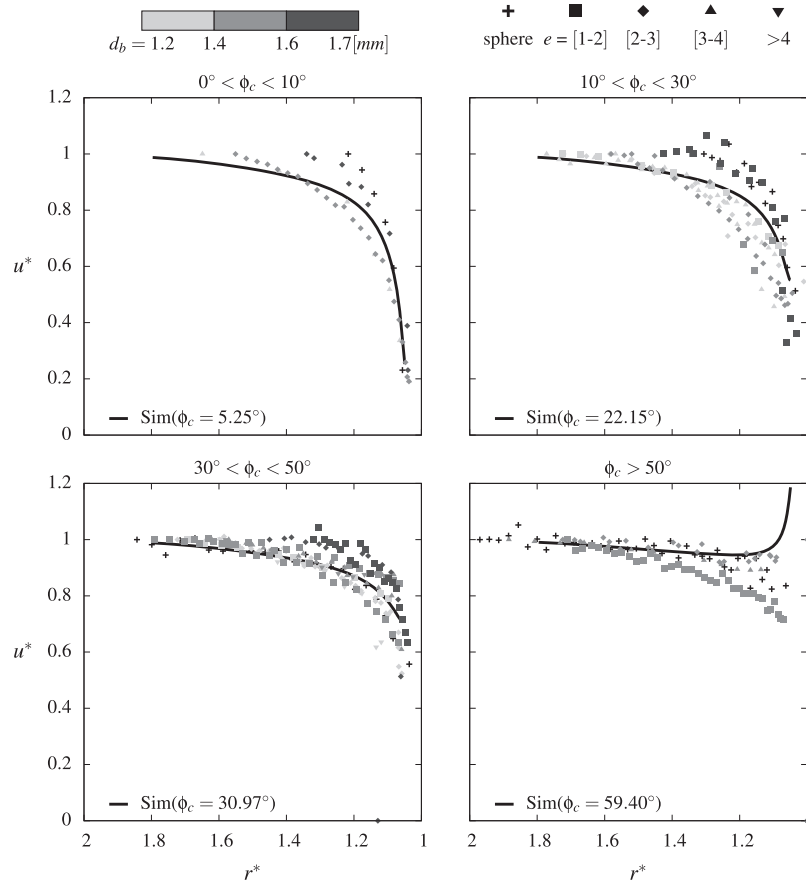


Fig. 6. Evolution of the particle velocity magnitude during the approach phase. The data are sorted by collision angles.

formulations are also simplified as a result of the small particle-to-bubble diameter ratio. The dimensionless capillary force, which tends to pull the solid particle into the gas phase, equals the product of the gas–liquid surface tension with the length of the three-phase contact line. Its formulation reads

$$\frac{F_{cap}(\phi = 180^\circ)}{2\pi\sigma L} = \frac{1}{2} \left(\frac{d_p}{L} \right) \sin \alpha \sin(\theta - \alpha). \quad (16)$$

For the exact definition of the angle α the reader is referred to the original work of [Nguyen \(2003\)](#). Typically the total adhesion force is maximum for $\alpha = 28^\circ$. Should the centrifugal force be introduced in the original force balance model of [Nguyen \(2003\)](#), the value of α , for which the adhesion force is maximum, will change. The force balance model of [Nutt \(1960\)](#) could for instance be employed. It has also been shown that, for a fixed particle volume, a prolate spheroid attaches even more strongly to a gas–liquid interface because of the larger particle–interface area ([Davies et al., 2014](#)). An exact solution of the various forces acting on the particle at the gas–bubble interface is however irrelevant in the present discussion since we only seek to compare their respective orders of magnitude. The hydrostatic pressure force of the liquid phase above the contact area at the gas–liquid interface is given by

$$\frac{F_h(\phi = 180^\circ)}{2\pi\sigma L} = \frac{1}{4} \left(\frac{d_p}{L} \right)^2 \left(\frac{d_b}{2L} - \frac{2L}{d_b} \right) \sin^2 \alpha. \quad (17)$$

The buoyancy force, which largely applies to the particle volume immersed in the liquid phase, is defined as

$$\frac{F_b(\phi = 180^\circ)}{2\pi\sigma L} = \frac{1}{48} \left(\frac{d_p}{L} \right)^3 (2 + 3 \cos \alpha - \cos^3 \alpha). \quad (18)$$

The particle weight is given by

$$\frac{F_g(\phi = 180^\circ)}{2\pi\sigma L} = \frac{1}{12} \left(\frac{d_p}{L} \right)^3 S. \quad (19)$$

Using the theoretical formulation of the centrifugal force derived by [Dai et al. \(1998\)](#), it can be shown that its magnitude is proportional to $\sin^2 \phi$, and therefore the centrifugal force reaches its theoretical maxima at the bubble equator $\phi = 90^\circ$. [Fig. 7](#) shows that the maximal sliding velocity roughly equals the terminal velocity. With a typical terminal velocity $u_\infty = 3$ mm/s ([Annex 1](#)) and an average bubble diameter $d_b = 1.4$ mm, a fair estimate of the centrifugal force at the equator can be given by

$$\frac{F_c(\phi = 90^\circ)}{2\pi\sigma L} = \frac{1}{12} \left(\frac{d_p}{L} \right)^3 S \left(\frac{2u_\infty^2}{gd_b} \right) \approx 10^{-3} \frac{1}{12} \left(\frac{d_p}{L} \right)^3 S. \quad (20)$$

For comparison purposes all the above forces were made function of the ratio of the particle diameter to the capillary length. With a capillary length of about $L = 2.7$ mm this ratio becomes very small, i.e. $d_p/L \ll 1$. The particle buoyancy (Eq. (18)) and the particle weight (Eq. (19)) are therefore two orders of magnitude smaller than the capillary force. The centrifugal force (Eq. (20)) is by even more orders of magnitude smaller than the capillary force. It therefore seems fair to neglect the effect of the centrifugal force on the change in the fibre orientation over the course of a weak attachment.

Terminal velocity of the elongated particles

In the present model it was assumed that the particles were spherical. However, the drag of an elongated particle does not necessarily equal that of an equivalent sphere. The terminal velocity

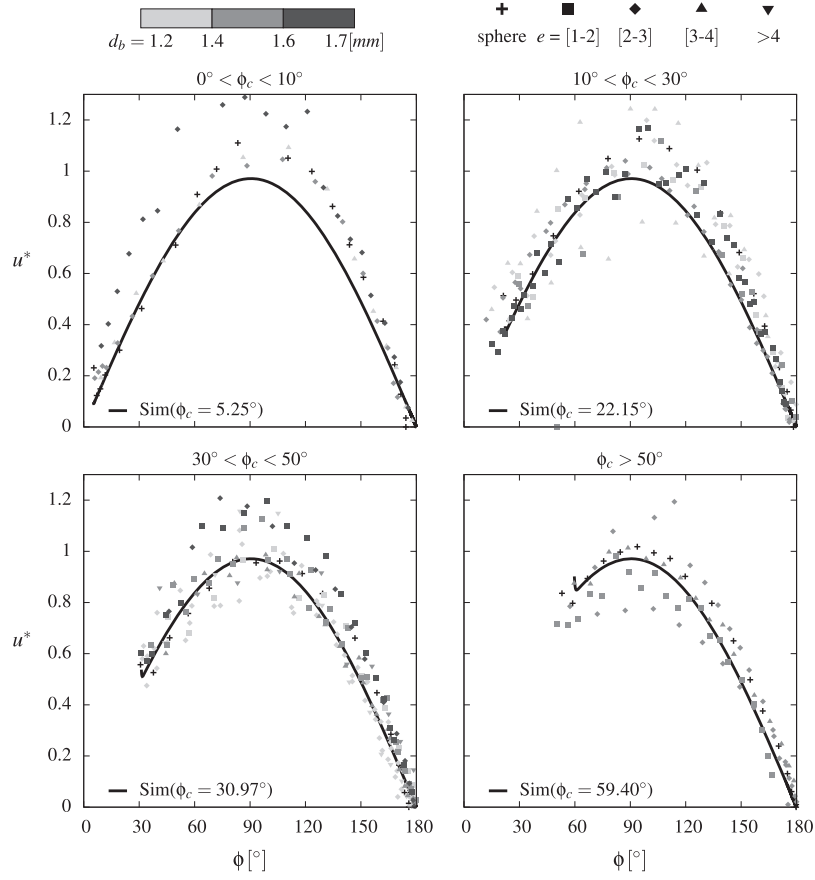


Fig. 7. Evolution of the particle velocity magnitude during the sliding phase. The data are sorted by collision angles.

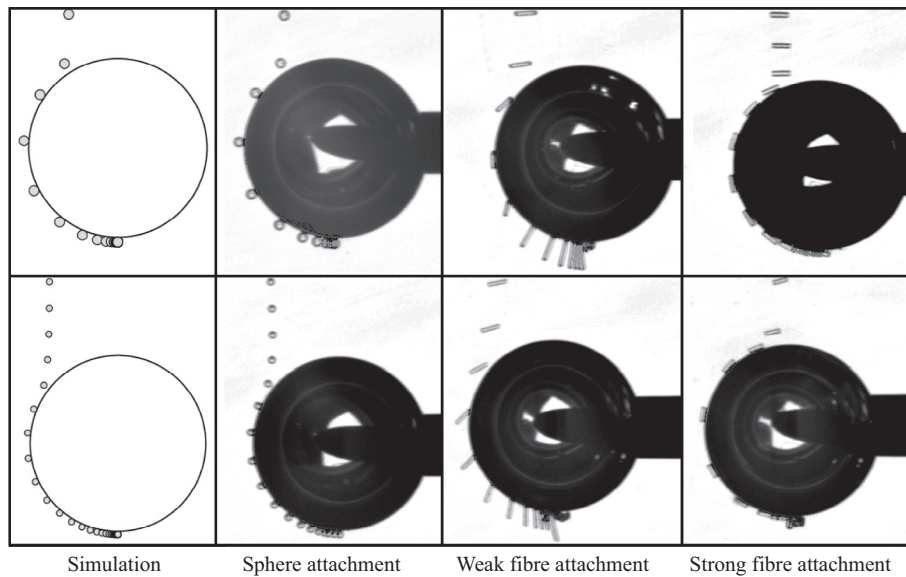


Fig. 8. Simulated attachment of a spherical particle, experimental attachment of a spherical particle, experimental weak attachment of an elongated particle and experimental strong attachment of an elongated particle (from left to right).

u_{∞}^{\parallel} of an elongated particle, which has its major axis parallel to the direction of motion (particle in a vertical position), will differ from the terminal velocity u_{∞}^{\perp} of the exact same particle descending with its major axis normal to the relative particle motion (particle

in a horizontal position). Therefore the two shape factors κ_{\parallel} and κ_{\perp} , defined as the ratio of the terminal velocity of an elongated particle to that of an equivalent sphere of same volume and density (Kasper et al., 1985) are normally introduced

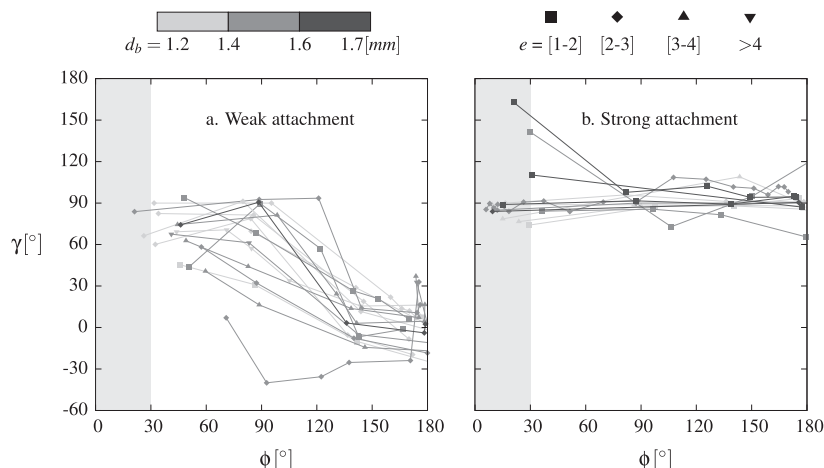


Fig. 9. About 90% of experimental runs, in which the collision angle exceeded the threshold $\phi_c > 30^\circ$, resulted in a weak attachment (a). Should the collision angle be lower than this threshold collision angle (grey area in b), the attachment takes a strong form.

Table 2

Estimations of the two shape factors of an elongated particle. The approximation is derived from the work of Loth (2008). The experimental values are measured from a falling chain of beads (Kasper et al., 1985).

	κ_{\parallel}	κ_{\perp}
Approximation ($1 < e < 6$)	$(\frac{4}{3} + \frac{e}{5})e^{-1/3}$	$(\frac{4}{3} + \frac{2e}{5})e^{-1/3}$
$e = 3$ (Approximation)	0.97	1.25
$e = 3$ (Experiment)	1.06	1.26
$e = 6$ (Approximation)	1.10	1.65
$e = 6$ (Experiment)	1.20	1.52

$$\kappa_{\parallel} = \frac{u_{\infty}^{\parallel}}{u_{\infty}^{eq}}, \quad \kappa_{\perp} = \frac{u_{\infty}^{\perp}}{u_{\infty}^{eq}}. \quad (21)$$

In the above formulation u_{∞}^{eq} corresponds to the terminal velocity of a sphere of equivalent volume. Exact, limiting and approximate solutions for the drag on spheroids at creeping flow conditions using the slender-body theory were derived by Oberbeck (1876). As is the case here, a creeping flow indicates that the Reynolds number based on the particle diameter and the liquid viscosity is lower than unity. One of the approximations (Loth, 2008), for which the aspect ratio of a needle-like ellipsoid (prolate) is greater than unity, can be found in Table 2. The shape factors are calculated for an aspect ratio of 3 and 6. The theoretical value is compared with the experimental data derived from the work of Kasper et al. (1985). For a particle aspect ratio of $e = 3$ one can expect a maximum difference in the terminal velocity of about 30% compared to that of an equivalent sphere. This difference will increase to about 60% for a particle aspect ratio equalled to $e = 6$. The present model, which involves spherical particles, therefore underestimates the translational velocities. It is however not directly shown in the figures since the velocity variables were made non-dimensional with the terminal velocity. The experimental determination of the terminal velocity was taken from the first two occurrences of the particle in the camera field of view. It was shown here that the particle velocity is affected within $r^* < 1.8$. Fig. 8 and the two videos available in the supplementary material show that some particles enter the field of view at an altitude of about $r^* \approx 1.5$. It is therefore likely that the terminal velocity does not always exactly correspond to the one, which would be observed at a higher altitude. Unfortunately there is no better alternative for determining the exact terminal velocity of the elongated particles.

Conclusions

The present work looked at the attachment of solid elongated particles on the surface of a stationary gas bubble immersed in stagnant water. It was shown that the particle aspect ratio has no significant effect on the translational velocities of the particles. The far-bubble region, in which the velocity of the particle is not affected by the bubble, was found to be the region in which the normalised polar radius was greater than $r^* > 1.8$. The results matched very well those obtained numerically with spheres as long as the collision angle remained lower than $\phi_c < 50^\circ$. For the first time the existence of two types of attachment has been shown. Upon collision near the upstream pole of the gas bubble the major axis of the fibre aligns with the local bubble surface (tangential fibre alignment, strong attachment). If collision occurs at least 30° further downstream only the head of the fibre is in contact with the gas–liquid interface (radial fibre alignment, weak attachment).

Acknowledgements

This work was supported by a Marie Curie International Outgoing Fellowship with the European Union Seventh Framework Program for Research and Technological Development (2007–2013) under the grant agreement number 623518.

Appendix A. Supplementary material

Supplementary data associated with this article can be found, in the online version, at <http://dx.doi.org/10.1016/j.ijmultiphaseflow.2015.01.002>.

References

- Ahmed, N., Jameson, G.J., 1985. The effect of bubble-size on the rate of flotation of fine particles. *Int. J. Miner. Process.* 14, 195–215.
- Albijanic, B., Ozdemir, O., Nguyen, A.V., Bradshaw, D., 2010. A review of induction and attachment times of wetting thin films between air bubbles and particles and its relevance in the separation of particles by flotation. *Adv. Colloid Interface Sci.* 159, 1–21.
- Brunauer, S., Emmett, P.H., Teller, E., 1938. Adsorption of gases in multimolecular layers. *J. Am. Chem. Soc.* 60, 309–319.
- Cho, Y.S., Laskowski, J.S., 2002. Effect of flotation frothers on bubble size and foam stability. *Int. J. Miner. Process.* 64, 69–80.
- Crowe, C.T., Schwarzkopf, J.D., Sommerfeld, M., Tsuji, Y., 2011. *Multiphase flows with droplets and particles*, second ed. CRC Press.

- Dai, Z., Dukhin, S., Fornasiero, D., Ralston, J., 1998. The inertial hydrodynamic interaction of particles and rising bubbles with mobile surfaces. *J. Colloid Interface Sci.* 197, 275–292.
- Das, S.C., Larson, I., Morton, D.A., Stewart, P.J., 2011. Determination of the polar and total surface energy distributions of particulates by inverse gas chromatography. *Langmuir* 27, 521–523.
- Davies, G.B., Kruger, T., Coveney, P.V., Harting, J., 2014. Detachment energies of spheroidal particles from fluid–fluid interfaces. *J. Chem. Phys.* 141, 154902.
- Forsberg, K.S.E., Subrahmanyam, T.V., Nilsson, L.K., 1993. Influence of grinding method on complex sulphide ore flotation: A pilot plant study. *Int. J. Miner. Process.* 38, 157–175.
- Fuerstenau, M.C., Jameson, G.J., Yoon, R.-H., 2007. Froth flotation: a century of innovation. Society for Mining, Metallurgy and Exploration, Inc. (SME).
- Gamble, J.F., Leane, M., Olusanmi, D., Tobyn, M., Supuk, E., Khoo, J., Naderi, M., 2012. Surface energy analysis as a tool to probe the surface energy characteristics of micronized materials—a comparison with inverse gas chromatography. *Int. J. Pharm.* 422, 238–244.
- Gu, G., Sean Sanders, R., Nandakumar, K., Xu, Z., Masliyah, J.H., 2004. A novel experimental technique to study single bubble–bitumen attachment in flotation. *Int. J. Miner. Process.* 74, 15–29.
- Huang, Z., Legendre, D., Guiraud, P., 2011. A new experimental method for determining particle capture efficiency in flotation. *Chem. Eng. Sci.* 66, 982–997.
- Huang, Z., Legendre, D., Guiraud, P., 2012. Effect of interface contamination on particle–bubble collision. *Chem. Eng. Sci.* 68, 1–18.
- Hubička, M., Basařová, P., Vejražka, J., 2013. Collision of a small rising bubble with a large falling particle. *Int. J. Miner. Process.* 121, 21–30.
- Jameson, G.J., 2010. Advances in fine and coarse particle flotation. *Can. Metall. Q.* 49, 325–330.
- Kasper, G., Niida, T., Yang, M., 1985. Measurements of viscous drag on cylinders and chains of spheres with aspect ratios between 2 and 50. *J. Aerosol Sci.* 16, 535–556.
- Kemper, M., 1999. State-of-the-art and new technologies in flotation deinking. *Int. J. Miner. Process.* 56, 317–333.
- Koh, P.T.L., Hao, F.P., Smith, L.K., Chau, T.T., Bruckard, W.J., 2009. The effect of particle shape and hydrophobicity in flotation. *Int. J. Miner. Process.* 93, 128–134.
- Kursun, H., Ulusoy, U., 2006. Influence of shape characteristics of talc mineral on the column flotation behavior. *Int. J. Miner. Process.* 78, 262–268.
- Lecrivain, G., Barry, L., Hampel, U., 2014. Three-dimensional simulation of multilayer particle deposition in an obstructed channel flow. *Powder Technol.* 258, 134–143.
- Lecrivain, G., Hampel, U., 2012. Influence of the lagrangian integral time scale estimation in the near wall region on particle deposition. *ASME J. Fluids Eng.* 134, 1–6.
- Legendre, D., Sarrot, V., Guiraud, P., 2009. On the particle inertia-free collision with a partially contaminated spherical bubble. *Int. J. Multiph. Flow* 35, 163–170.
- Loth, E., 2008. Drag of non-spherical solid particles of regular and irregular shape. *Powder Technol.* 182, 342–353.
- Mohammadi-Jam, S., Waters, K.E., 2014. Inverse gas chromatography applications: a review. *Adv. Colloid Interface Sci.* 212, 21–44.
- Nguyen, A.V., 2003. New method and equations for determining attachment tenacity and particle size limit in flotation. *Int. J. Miner. Process.* 68, 167–182.
- Nguyen, A.V., Jameson, G.J., 2005. Sliding of fine particles on the slip surface of rising gas bubbles: resistance of liquid shear flows. *Int. J. Multiph. Flow* 31, 492–513.
- Nguyen, P.T., Nguyen, A.V., 2009. Validation of the generalised sutherland equation for bubble–particle encounter efficiency in flotation: effect of particle density. *Miner. Eng.* 22, 176–181.
- Nowak, E., Robbins, P., Combes, G., Stitt, E.H., Pacek, A.W., 2013. Measurements of contact angle between fine, non-porous particles with varying hydrophobicity and water and non-polar liquids of different viscosities. *Powder Technol.* 250, 21–32.
- Nutt, C.W., 1960. Froth flotation – the adhesion of solid particles to flat interfaces and bubbles. *Chem. Eng. Sci.* 12, 133–141.
- Oberbeck, A., 1876. Über stationäre flüssigkeitsbewegungen mit berücksichtigung der inneren reibung. *Journal für die reine und angewandte Mathematik* 81, 62–81.
- Rahimi, M., Dehghani, F., Rezai, B., Aslani, M.R., 2012. Influence of the roughness and shape of quartz particles on their flotation kinetics. *Int. J. Miner. Metall. Mater.* 19, 284–289.
- Ralston, J., Fornasiero, D., Hayes, R., 1999. Bubble–particle attachment and detachment in flotation. *Int. J. Miner. Process.* 56, 133–164.
- Ren, Y., Wu, Z., Ondruschka, B., Braeutigam, P., Franke, M., Nehring, H., Hampel, U., 2011. Oxidation of phenol by microbubble-assisted microelectrolysis. *Chem. Eng. Technol.* 34, 699–706.
- Rosenqvist, T., 2004. Principles of Extractive Metallurgy. Tapir Academic Press.
- Rubio, J., Souza, M.L., Smith, R.W., 2002. Overview of flotation as a wastewater treatment technique. *Miner. Eng.* 15, 139–155.
- Sarrot, V., Guiraud, P., Legendre, D., 2005. Determination of the collision frequency between bubbles and particles in flotation. *Chem. Eng. Sci.* 60, 6107–6117.
- Schindelin, J., Arganda-Carreras, I., Frise, E., Kaynig, V., Longair, M., Pietzsch, T., Preibisch, S., Rueden, C., Saalfeld, S., Schmid, B., Tinevez, J.-Y., White, D.J., Hartenstein, V., Eliceiri, K., Tomancak, P., Cardona, A., 2012. Fiji: an open-source platform for biological-image analysis. *Nat. Methods* 9, 676–682.
- Schulze, H.J., 1989. Hydrodynamics of bubble–mineral particle collisions. *Miner. Process. Extr. Metall. Rev.* 5, 43–76.
- Schulze, H.J., 1992. Probability of particle attachment on gas bubbles by sliding. *Adv. Colloid Interface Sci.* 40, 283–305.
- Susana, L., Campaci, F., Santomaso, A.C., 2012. Wettability of mineral and metallic powders: Applicability and limitations of sessile drop method and washburn's technique. *Powder Technol.* 226, 68–77.
- Tao, D., 2005. Role of bubble size in flotation of coarse and fine particles—a review. *Sep. Sci. Technol.* 39, 741–760.
- Tino, E., Dieter, W., Lama, N., Klaus, A., 1996. Dehydration of glass surfaces studied by contact angle measurements. *J. Colloid Interface Sci.* 179, 635–636.
- van Oss, C.J., 2003. Long-range and short-range mechanisms of hydrophobic attraction and hydrophilic repulsion in specific and aspecific interactions. *J. Mol. Recognit.* 16, 177–190.
- van Oss, C.J., Giese, R.F., Docoslis, A., 2005. Hyperhydrophobicity of the water–air interface. *J. Dispersion Sci. Technol.* 26, 585–590.
- VDI-GVC, 2013. Verein Deutscher Ingenieure (VDI) – Gesellschaft Verfahrenstechnik und Chemieingenieurwesen (GVC), *Wärmeatlas*, 11th ed. VDI-Verlag, Springer.
- Verrelli, D.I., Bruckard, W.J., Koh, P.T.L., Schwarz, M.P., Follink, B., 2014. Particle shape effects in flotation. Part 1: microscale experimental observations. *Miner. Eng.* 58, 80–89.
- Verrelli, D.I., Koh, P.T.L., Bruckard, W.J., Schwarz, M.P., 2012. Variations in the induction period for particle–bubble attachment. *Miner. Eng.* 36–38, 219–230.
- Verrelli, D.I., Koh, P.T.L., Nguyen, A.V., 2011. Particle–bubble interaction and attachment in flotation. *Chem. Eng. Sci.* 66, 5910–5921.
- Wang, W., Zhou, Z., Nandakumar, K., Xu, Z., Masliyah, J.H., 2003a. Attachment of individual particles to a stationary air bubble in model systems. *Int. J. Miner. Process.* 68, 47–69.
- Wang, W., Zhou, Z., Nandakumar, K., Xu, Z., Masliyah, J.H., 2003b. Effect of surface mobility on the particle sliding along a bubble or a solid sphere. *J. Colloid Interface Sci.* 259, 81–88.
- Ye, Y., Khandrika, S.M., Miller, J.D., 1989. Induction-time measurements at a particle bed. *Int. J. Miner. Process.* 25, 221–240.
- Yekeler, M., Ulusoy, U., Hıçyılmaz, C., 2004. Effect of particle shape and roughness of talc mineral ground by different mills on the wettability and floatability. *Powder Technol.* 140, 68–78.
- Yoon, R.H., Luttrell, G.H., 1989. The effect of bubble size on fine particle flotation. *Miner. Process. Extr. Metall. Rev.* 5, 101–122.